The disordered C-terminal tail of fungal LPMOs from phytopathogens mediates protein dimerization and impacts plant penetration

Ketty Tamburrini, Sayo Kodama, Sacha Grisel, Mireille Haon, Takumi Nishiuchi, Bastien Bissaro, Yasuyuki Kubo, Sonia Longhi, Jean-Guy Berrin

PNAS RESEARCH ARTICLE | BIOCHEMISTRY

The disordered C-terminal tail of fungal LPMOs from phytopathogens mediates protein dimerization and impacts plant penetration

Ketty C. Tamburrini[a,b], Sayo Kodama[c], Sacha Grisel[b,d], Mireille Haon[b,d], Takumi Nishiuchi[e], Bastien Bissaro[b], Yasuyuki Kubo[c], Sonia Longhi[a,1], and Jean-Guy Berrin[b,1]

Edited by Amy Rosenzweig, Northwestern University, Evanston, IL; received November 20, 2023; accepted February 13, 2024

Lytic polysaccharide monooxygenases (LPMOs) are monocopper enzymes that oxidatively degrade various polysaccharides, such as cellulose. Despite extensive research on this class of enzymes, the role played by their C-terminal regions predicted to be intrinsically disordered (dCTR) has been overlooked. Here, we investigated the function of the dCTR of an LPMO, called *Co*AA9A, up-regulated during plant infection by *Colletotrichum orbiculare*, the causative agent of anthracnose. After recombinant production of the full-length protein, we found that the dCTR mediates *Co*AA9A dimerization in vitro, via a disulfide bridge, a hitherto-never-reported property that positively affects both binding and activity on cellulose. Using SAXS experiments, we show that the homodimer is in an extended conformation. In vivo, we demonstrate that gene deletion impairs formation of the infection-specialized cell called appressorium and delays penetration of the plant. Using immunochemistry, we show that the protein is a dimer not only in vitro but also in vivo when secreted by the appressorium. As these peculiar LPMOs are also found in other plant pathogens, our findings open up broad avenues for crop protection.

plant cell wall | cellulose | fungal pathogen | oxidative enzyme | intrinsically disordered region

Significance

Lytic polysaccharide monooxygenases (LPMOs) are oxidative enzymes that revolutionized our vision of plant cell wall polysaccharides degradation, and their involvement in a myriad of other biological processes is only starting to unfold. So far, most studies have focused on their diversity, catalytic mechanism, and substrate specificities. However, the function of their C-terminal regions predicted to be disordered is still unknown. Using a multidisciplinary approach, we provide experimental evidence of the disordered nature of these C-terminal tails and found that some of them can drive disulfide-bridge-mediated LPMO dimerization, positively modulating binding to cellulose and activity. The key role of these secreted oxidative enzymes in pathogenicity is supported by gene deletion studies and their widespread occurrence in fungal pathogens.

Lytic polysaccharide monooxygenases (LPMOs) are monocopper enzymes that revolutionized our understanding of the enzymatic mechanisms involved in the degradation of polysaccharides. LPMOs cleave glycosidic bonds through oxidative reactions (1, 2), acting at the surface of recalcitrant substrates in concert with other carbohydrate-active enzymes (CAZymes) (3–6). Their unique catalytic properties attracted growing attention both fundamentally (7) and for their biotechnological potential, e.g., for biofuels and nanocellulose production (6, 8). LPMOs are widely distributed across all domains of life, particularly abundant in bacterial and fungal communities. Recent studies have unveiled their multiple roles in different biological contexts (9), with for instance roles proposed in the cell wall remodeling of insects (10) or fungi (11), and demonstrated functions as virulence factors in pathogenic bacteria (12), viruses (13), oomycetes (14), and fungi (15).

LPMOs are distributed into eight auxiliary activity (AA) families in the CAZy database (AA9 to AA11 and AA13 to AA17) (16) and are mainly active on cellulose, chitin, xylan, starch, or pectin, although the substrate specificity varies among the families. Interestingly, LPMOs from the AA9 family are very abundant in fungal genomes, with some filamentous fungi encoding more than 60 AA9s (17), though the reason for this redundancy remains unknown. AA9 LPMOs specifically oxidize carbon atoms 1 and/or 4 (C1 and/or C4) of the scissile glycosidic bond in the backbone of polymers such as cellulose, cello-oligosaccharides, or hemicelluloses (18–20). The typical AA9 LPMO structure consists of a well-conserved immunoglobulin-like β-sandwich fold with a flat binding surface that exposes a monocopper atom coordinated by a strictly conserved pair of histidine residues (21, 22), so-called "histidine brace" (23). This rare structural motif is formed by the amino group and side chain of the N-terminal histidine with the nitrogen from a second histidine side chain to give a T-shaped copper coordination geometry. To catalyze their reaction, the active-site copper ion has to be reduced from Cu(II) to Cu(I). This process requires an electron source, which can be provided by a variety of small molecules, such as ascorbic acid, or redox enzymes, such as cellobiose dehydrogenase (CDH) (5, 24). Then, the reduced enzyme reacts with H_2O_2 (or O_2 in some proposed alternative pathways) to catalyze the abstraction of hydrogen atoms from C1 or C4 atoms of the substrate, followed by hydroxylation which induces glycosidic bond cleavage (2, 25).

The catalytic domain of LPMOs can be found either as a single isolated domain, or followed by either a carbohydrate-binding module (CBM), which promotes binding to the substrate (26), or by glycosylphosphatidylinositol (GPI) anchors, or by a region of

Author contributions: K.C.T., S.L., and J.-G.B. designed research; K.C.T., S.K., S.G., M.H., and T.N. performed research; S.L. and J.-G.B. contributed new reagents/analytic tools; K.C.T., S.K., T.N., B.B., Y.K., S.L., and J.-G.B. analyzed data; and K.C.T., B.B., S.L., and J.-G.B. wrote the paper.

The authors declare no competing interest.

This article is a PNAS Direct Submission.

[1]To whom correspondence may be addressed. Email: sonia.longhi@univ-amu.fr or jean-guy.berrin@inrae.fr.

This article contains supporting information online at https://www.pnas.org/lookup/suppl/doi:10.1073/pnas.2319998121/-/DCSupplemental.

Published March 21, 2024.

unknown function (27). We have recently shown using bioinformatic approaches that a significant proportion of such "unknown" regions are predicted to be intrinsically disordered in most LPMO families (28). For instance, such disordered C-terminal regions (dCTRs) occur in ~23% of AA9 members. Intrinsically disordered regions (IDRs) are usually very challenging to study as they do not adopt a well-defined conformation due to the lack of stable secondary and/or tertiary structure in the absence of partners or ligands, existing as dynamic ensembles of conformations (29, 30). IDRs are capable of fulfilling their function either by maintaining complete disorder or by undergoing a disorder-to-order transition upon interaction with their biological effectors, which is referred to as "induced folding" (30). Several studies demonstrated that IDRs play key roles in eukaryotes, by regulating, among others, signal transduction, transcriptional regulation, and cell growth (31). Due to their flexibility, IDRs can tune several enzymatic properties, such as the affinity for different substrates, allostery and catalysis, stability, subcellular localization, and enzyme processivity (32–34).

To date, the function of dCTRs in LPMOs remains unknown. This is most probably because functional studies focused on the LPMO catalytic domain and that the dCTR-encoding sequence is usually removed during cloning. In this study, with the goal of contributing to fill this knowledge gap, we focused on the ascomycete *Colletotrichum orbiculare* that displays several AA9-dCTRs. Species belonging to the *Colletotrichum* genus are among the top 10 fungal pathogens worldwide, endangering plant health and causing major crop production losses (35). They infect the host by developing an appressorium infection structure with the concomitant secretion of CAZymes to penetrate the plant cell wall tissue (36, 37). Among this arsenal of enzymes, we show that *C. orbiculare* fine-tunes the expression of several AA9s during infection, including AA9-dCTRs. Using a combination of biochemical and biophysical approaches, together with reverse genetics, we elucidated the role of some of these intriguing regions found in AA9 LPMOs from fungal phytopathogens.

Results

C-terminal Disordered Regions Are Abundant in *C. orbiculare* AA9 LPMOs. To get insight into the role of the dCTR in AA9 LPMOs, we first analyzed the 27 AA9 sequences of the fungal pathogen *C. orbiculare* (*Co*AA9) (Fig. 1). Among these sequences, 12 possess a single AA9 domain while five harbor a C-terminal CBM and 10 display an AA9 domain followed by a dCTR as predicted by IUPred2A (38) (Fig. 1*A*). The dCTR sequences from *C. orbiculare* vary in length (between 24 and 179 residues; *SI Appendix*, Fig. S1*A*) with a high fraction of predicted disordered residues (median value of 100%; *SI Appendix*, Fig. S1*B*). Despite different patterns of distribution of oppositely charged residues (*SI Appendix*, Fig. S1*C*), most dCTRs share a patch of highly positively charged residues at the end of the sequence (Fig. 1*B*). Among them, we noticed that some *Co*AA9-dCTR sequences present a conserved, positively charged short linear motif [SLiM; (39)], identified by the consensus motif "RXHAR," and previously annotated as module X283 in the CAZy database by Lenfant et al. (27). A phylogenetic analysis of the catalytic domains of all the AA9 sequences harboring this X283 motif within the *Colletotrichum* genus revealed that the *Co*AA9-X283 sequences cluster into two clearly distinct clades (Fig. 1*B*). Looking at the dCTR appended to the catalytic domains of these AA9 sequences in each of the two clades, we noticed that this segregation of AA9 domains seems to be correlated with a divergence of the sequence properties of the last 26 residues of their dCTRs. Indeed, while both clades present a conserved Cys preceding the X283 motif, the consensus sequence of clade B is strictly conserved, while the consensus sequence of clade A is more variable. Importantly, most *Colletotrichum* species have two AA9-X283, with at least one in each of the two clades, suggesting a selection pressure to maintain a functional divergence.

Biochemical Characterization of *Co*AA9-dCTR LPMOs Unveils a Cys-Driven Dimerization. To get functional insights into the dCTR of *Co*AA9 LPMOs, the two AA9-dCTRs of *C. orbiculare*, *viz.* *Co*AA9A and *Co*AA9B, were selected for functional characterization based on the specific features of their dCTRs and their upregulation during pathogenesis (vide infra). While we were expecting some difficulties in protein expression due to the presence of the disordered region, both enzymes were successfully produced by *Pichia pastoris* and secreted into the supernatant from which they could be purified without using any C-terminal tag. Intriguingly, during the purification of *Co*AA9A, the size exclusion chromatography (SEC) elution profile showed two peaks (Fig. 2*A*). Further analyses of the two peaks using SEC with multi-angle laser light scattering (MALLS) detector, a technique enabling estimation of the total molecular mass and of the relative protein and sugar content, unveiled that they consist of glycosylated species, with a total molecular mass of 71 kDa (peak #1) and 35 kDa (peak #2) (*SI Appendix*, Fig. S2 *A* and *B* and Table S1). After elution, we also noticed that both species were stable, i.e. once isolated they do not spontaneously interconvert into each other. SDS-PAGE analysis showed that peak #1 migrates at an apparent molecular mass of ~95 kDa in the absence of reducing agents, while the band was shifted toward ~50 kDa in the presence of DTT (*SI Appendix*, Fig. S3), suggesting that peak #1 corresponds to a dimeric species driven by the formation of a disulfide bridge between two Cys residues. *Co*AA9A displays five cysteines, four in the catalytic domain and only one in the C-terminal region (Fig. 2*B*). The AlphaFold2 model (41) of *Co*AA9A predicts two disulfide bridges, one between Cys59 and Cys176, conserved among all structurally determined AA9 LPMOs, and another one between Cys100 and Cys104 (Fig. 2*B*). Therefore, we reasoned that the fifth cysteine, Cys266, could be the residue responsible for *Co*AA9A dimerization. To investigate its potential contribution to the dimerization, we mutated Cys266 into an Ala and found that the dimerization was abolished in the C266A variant (Fig. 2*C* and *SI Appendix*, Fig. S2*C* and Table S1). We also produced a truncated variant of *Co*AA9A (henceforth called ΔX283) lacking the last 26 residues (aa 257 to 283), immediately after the last predicted *O*-glycosylation site. This truncation, which removed Cys266, also abolished the ability of *Co*AA9A to dimerize (Fig. 2*D*). Of note, the molecular size of this variant (24 kDa) is smaller than expected (27 kDa) (*SI Appendix*, Fig. S2*D* and Table S1), consistent with a proteolytic degradation of the dCTR.

Cys266 is preceded by negatively charged residues and followed by positively charged ones, hinting at a possible role of charges in promoting dimerization (Fig. 1*B*). In order to test this hypothesis, we reduced Cys266 in *Co*AA9A monomer with DTT, and then performed different SEC analyses in the presence of increasing salt concentrations (*SI Appendix*, Fig. S4). The dimer/monomer ratio was found to decrease with increasing salt concentrations, confirming that electrostatic interactions promote the dimerization. Interestingly, we show that *Co*AA9B, which also displays a conserved Cys (Cys298) in the dCTR, is able to dimerize (*SI Appendix*, Fig. S5*A*). However, the dimer/monomer proportion is lower than in the case of *Co*AA9A, suggesting that Cys298 is either less accessible to intermolecular interactions than Cys266 from *Co*AA9A or that the electrostatics is less favorable.

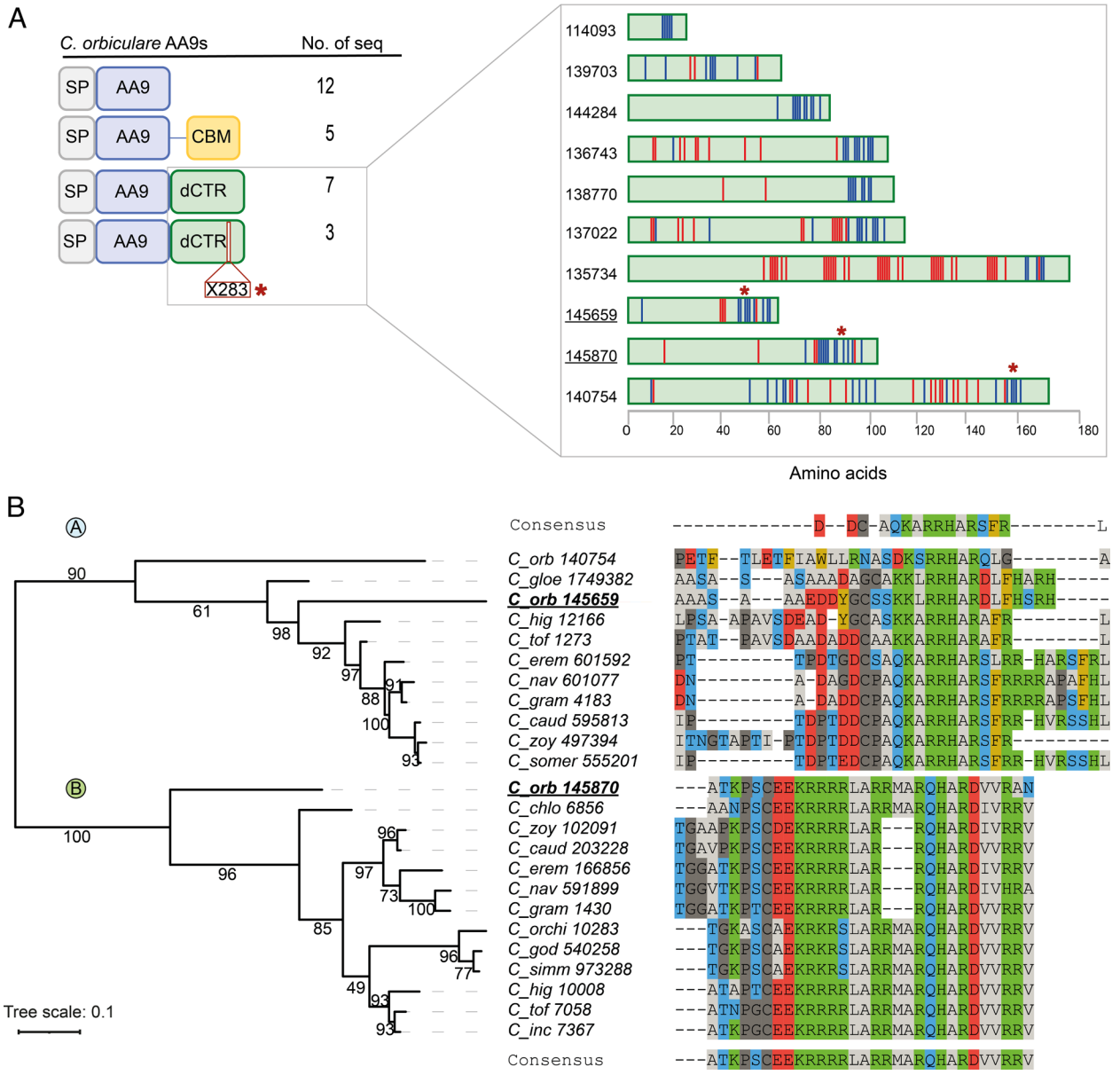

Fig. 1. In silico analyses of the dCTRs occurring in *Colletotrichum* AA9 LPMOs. (*A*) Modular architecture of the 27 AA9 sequences from *C. orbiculare* as defined by InterPro; dCTRs were identified by the IUPred2A disorder predictor (38). The *Inset* shows the length of each dCTR (with JGI identifier indicated for each dCTR-containing sequence) and the vertical colored bars within each dCTR represent the distribution of charged residues along the sequence, where Asp and Glu residues are colored in red, while Arg, Lys, and His residues are colored in blue. The red stars indicate the X283 motif. (*B*) Phylogenetic tree of the catalytic domains of AA9s bearing the X283 motif within the *Colletotrichum* genus (100 bootstraps, values shown next to each node). Numbers indicate the JGI identifier of each sequence (40). Adjacent to each clade, the multiple sequence alignment of the last residues within the dCTR and the consensus sequence are shown. The enzymes studied in the present work, *Co*AA9A (*C_orb* 145659) and *Co*AA9B (*C_orb* 145870) are underlined in panels (*A* and *B*).

While based on the AlphaFold2 model of *Co*AA9B (*SI Appendix*, Fig. S5*B*), Cys298 seems to be as accessible to the solvent as Cys266 of *Co*AA9A, we noticed that contrary to *Co*AA9A, Cys 298 of CoAA9B is not preceded by charged residues and is rather followed by a patch of oppositely charged residues (Fig. 1*B*). This would create a different local electrostatic environment that might be less favorable to dimerization. Therefore, we focused our efforts on *Co*AA9A, which displays a pronounced propensity to dimerization.

SEC-SAXS Analysis Supports Formation of a Dimer in Which the Extended dCTRs Are Engaged in a Disulfide-Bond. To get deeper structural insights, we analyzed *Co*AA9A by SEC coupled to small-angle X-ray scattering, a technique that provides information about size, shape, and oligomeric state of a protein in solution. Linearity of the Guinier region in the scattering curves of the dimer and of the monomer (Fig. 3*A*) enabled meaningful estimation of the radius of gyration (R_g). The derived R_g values are 30.2 Å ± 0.1 Å and 47.8 Å ± 0.2 Å for the monomer and the dimer, respectively. Both R_g values are bigger than the ones expected for folded proteins of the same length, as calculated from Flory's equation (see experimental section) (19 Å and 23 Å, respectively) and also bigger than the R_g computed from the AlphaFold2 models (27.3 Å and 34.1 Å, respectively). The pairwise distance distribution function of the monomer has an asymmetric shape and a long decline with a maximum intramolecular distance (D_{max}) of 120 Å, suggesting an elongated conformation (Fig. 3*B*). The dimer has a D_{max} of 217 Å and its P(r) function is characterized by two peaks, one at 25 Å, corresponding to the maximal intradomain distance, and a second peak at 63 Å corresponding to the interdomain distance followed

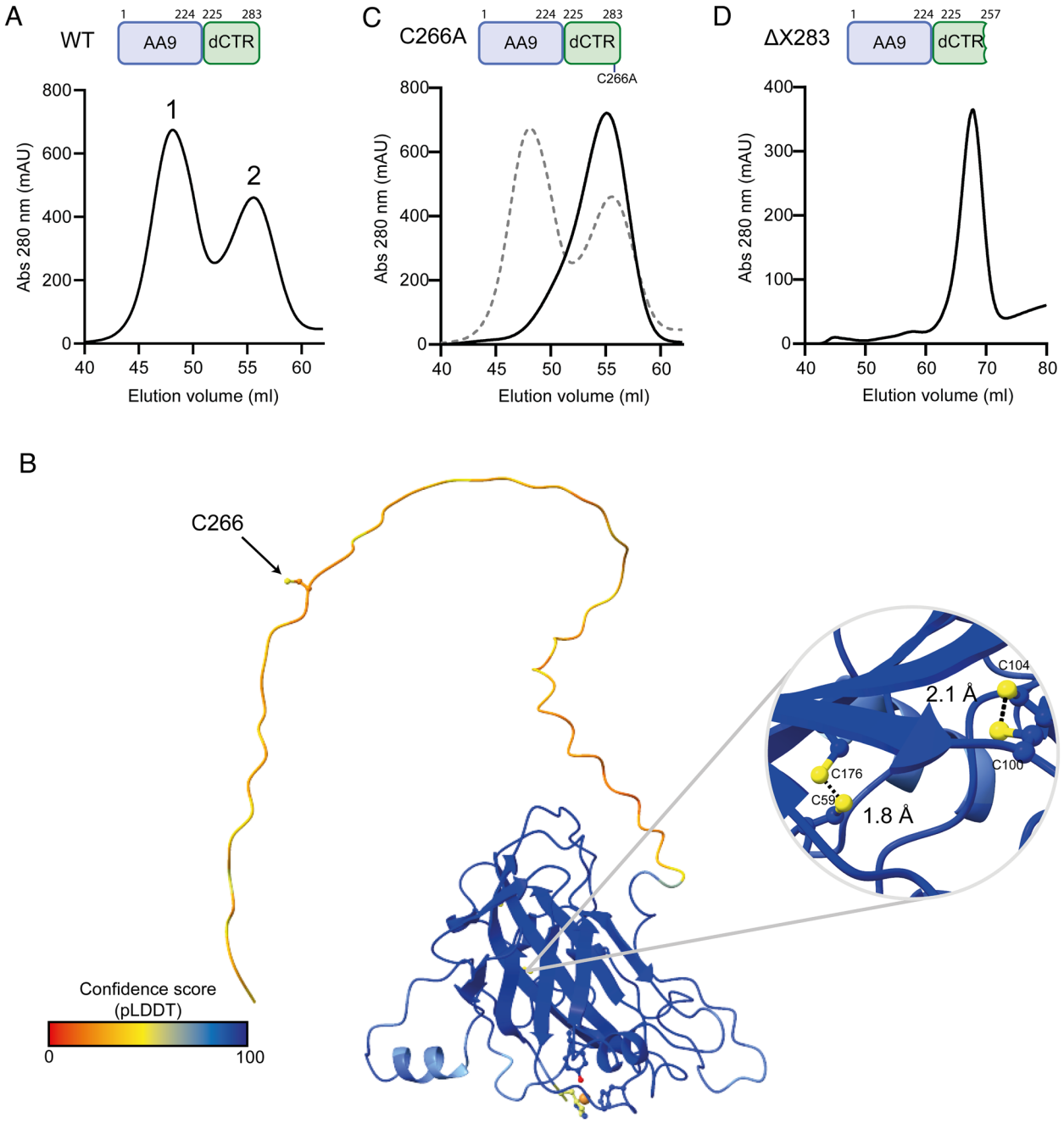

Fig. 2. Oligomerization status of *Co*AA9A WT, C266A, and ΔX283 variants. (*A*) SEC profile of full-length *Co*AA9A. Peaks #1 and #2 indicate the elution of the dimer and the monomer, respectively. (*B*) AlphaFold2 model of *Co*AA9A (41). The model is colored according to pLDDT values (pLDDT < 70: low confidence; pLDDT > 70: confident; pLDDT > 90: high confidence). The inset shows the distances between the two pairs of cysteines (shown as sticks), Cys59/Cys176 and Cys100/Cys104, located in the catalytic domain. Cys266, occurring in the dCTR and involved in the dimerization, is also labeled. (*C* and *D*) SEC profile of *Co*AA9A (dotted gray line) and the *Co*AA9A variants C266A (black line) (*C*) and ΔX283 lacking residues 257 to 283 (*D*).

by a long tail, typical of proteins containing globular domains tethered by long disordered regions (42) (Fig. 3*B*).

To qualitatively compare the flexibility of *Co*AA9A dimer and monomer, we employed the normalized Kratky plot (Fig. 3*C*). Both plots display a typical bell shape suggesting that both monomer and dimer are folded. However, a globular protein would have its maximum in the dimensionless Kratky plot around $qR_g = 1.73$, while the monomer has a maximum at $qR_g \approx 3$ and the dimer has a maximum at $qR_g \approx 5$. This indicates that they contain extended regions and that the dimer is more flexible than the monomer. We used ensemble optimization method (EOM) to achieve further insights into the conformational properties of the dimer (Fig. 3*D* and *SI Appendix*, Fig. S5). The best fit ($\chi^2 = 2.25$) (*SI Appendix*, Fig. S6*A*) was obtained by a combination of 14 conformations, represented by four models in Fig. 3*D*. Note that the relatively high χ^2 value is due to protein glycosylation: Indeed, glycans could not be included in the EOM modeling, thereby leading to a discrepancy between experimental and back-calculated scattering. The average R_g and size distributions (46 Å and 142 Å, respectively) are similar to those of the initial pool generated by EOM (47 Å and 141 Å, respectively) (*SI Appendix*, Fig. S6 *B* and *C*). The degree of flexibility can be assessed quantitatively by comparing the Rflex value of the selected sub-ensemble of conformers to that of the initial pool (where Rflex approaches 100% for a fully flexible system and 0% for a fully rigid system). The Rflex value of the selected sub-ensemble is 81.1% (to be compared to 86.4% for the initial

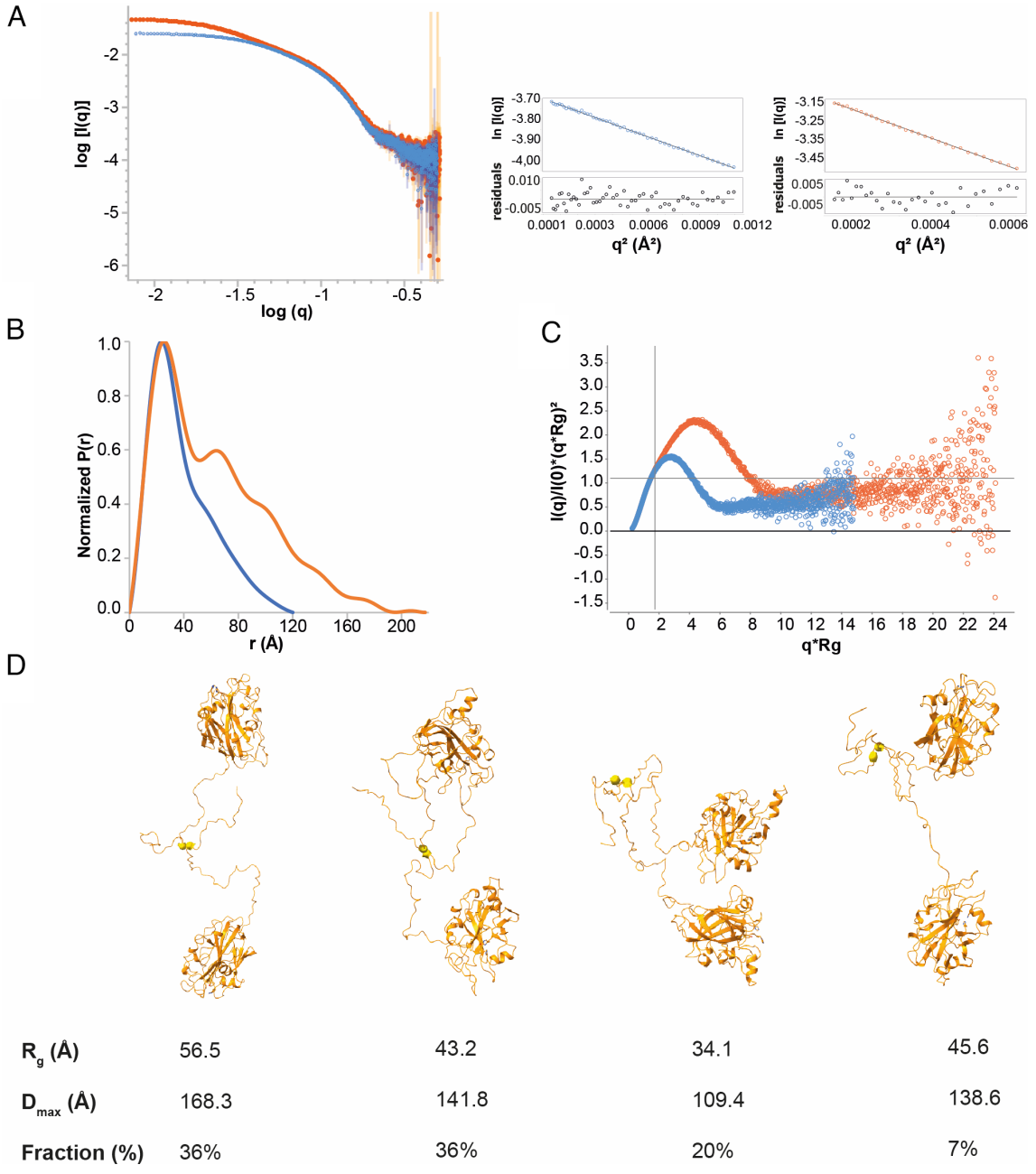

Fig. 3. Structural analysis of *Co*AA9A monomer and dimer by SEC-SAXS. (*A*) Log–log plot of the SAXS data of *Co*AA9A monomer (blue) and dimer (orange). The insets on the *Right* show the Guinier plots (*Top*) of the monomer (blue, *Left*) and of the dimer (orange, *Right*) along with the plot of residuals (*Bottom*). (*B*) Pairwise distance distribution function of *Co*AA9A monomer (blue) and dimer (orange). (*C*) Dimensionless Kratky plot of monomer (blue) and dimer (orange). The cross-hair marks the Guinier–Kratky point (1.732, 1.1), the main peak position for globular proteins. (*D*, *Upper*) representative conformations of the *Co*AA9A dimer ensemble generated by EOM. The catalytic domains were modeled with AlphaFold2 and used as rigid bodies in the EOM modeling. The distance between C266 in the two chains was fixed between 5 Å and 6 Å. The Cys residues in the dCTR are shown as golden spheres. (*Lower*) R_g and D_{max} values of the four representative models and their relative abundance in the ensemble.

pool) (Rsigma = 1.01), indicating that the system is highly flexible. Interestingly, while the AlphaFold2 model of the dimer is unable to predict the disulfide bridge and rather predicts that the two catalytic domains would face each other (*SI Appendix*, Fig. S7), SAXS data are consistent with a conformation in which the two catalytic domains are far away from each other but tethered together by the dCTR, as also shown by the ab initio reconstruction of *Co*AA9A dimer structure obtained with GASBOR (43) (*SI Appendix*, Fig. S8). An extended conformation is also consistent with the enzymatic assay results (vide infra).

We also analyzed by SEC-SAXS the C266A and ΔX283 variants. The C266A variant adopts a conformation similar to that of the monomer, as judged from its estimated R_g and D_{max} values (29.7 Å and 116 Å) as well as from the shape of the pair distance distribution function (*SI Appendix*, Fig. S9 *A* and *B*). By contrast, the ΔX283 variant has quite distinct conformational properties (*SI Appendix*, Fig. S8*C*): its estimated R_g value (18 Å) is lower than that observed for both *Co*AA9 WT and C266A variant and consistent with the values expected for a globular protein (18 Å). Likewise, its estimated D_{max} value is lower (63 Å), and the shape of the pair distance distribution function is symmetrical (*SI Appendix*, Fig. S9*D*), consistent with a globular conformation likely corresponding to the catalytic domain of *Co*AA9A alone, and reflecting degradation of the dCTR as already hypothesized

based on the SEC profile (Fig. 2*D*). Analysis of the normalized Kratky plots further supports the globular conformation of the ΔX283 variant, while both WT and C266A monomeric forms of *Co*AA9A contain extended regions (*SI Appendix*, Fig. S9*E*).

In conclusion, SEC-SAXS data experimentally confirm the disordered nature of the dCTR with the presence of extended regions in both the WT monomer and dimer (and also in C266A). They also reveal the persistence of disorder in the dimer with conformations compatible with a disulfide bridge-mediated dimerization.

The Dimerization Impacts Activity of *Co*AA9A on Cellulose. To investigate the impact of the dimerization on enzyme activity, we tested the isolated monomeric and dimeric forms of *Co*AA9A on cellulose. We found that both the monomer and the dimer display activity on cellulose, with the release of a mixture of neutral, C1-, and C4-oxidized cello-oligosaccharides (*SI Appendix*, Fig. S10). Interestingly, the amounts of C1- and C4-oxidized oligosaccharides were found to be significantly higher for the dimer compared to the monomer (Fig. 4*A*). The difference between monomer and dimer was observed both with ascorbic acid (Fig. 4*A*) and CDH used as electron-donors (*SI Appendix*, Fig. S11). In control experiments, the copper content, as determined using inductively coupled plasma-mass-spectrometry (ICP-MS), was in line with expectations for both monomer and dimer (i.e. ~1.3 and ~0.9 copper atom per catalytic domain, respectively). The melting temperatures (T_m), as determined by differential scanning fluorimetry, were also similar for the monomer (T_m = 51.5 °C) and the dimer (T_m = 52.0 °C) (*SI Appendix*, Fig. S12). Interestingly, the mutations mentioned above (ΔX283 and C266A) led both to a significantly lower ($P < 0.01$) activity on cellulose than that of the WT monomer (*SI Appendix*, Fig. S13). Following the release of C1 oxidized oligosaccharides by *Co*AA9A monomer and dimer over time, we found that the product formation rapidly increases and reaches a plateau after only 20 min for the monomer and 40 min for the dimer (Fig. 4*B*). Given that LPMO activity/stability and substrate binding are intimately related, we checked the impact of the dimerization on the binding to cellulose using pull-down assays. In the absence of ascorbic acid, no binding was detected. As the reduction of the active-site copper is known to initiate substrate binding (44), we carried out experiments in the presence of ascorbate that triggered binding to cellulose with clear differences between the monomer and the dimer (Fig. 4*C*). After only 5 min of incubation with cellulose, most of the dimer was bound (87%) while more than half of the monomer (58%) remained unbound. It is known that poor substrate binding often leads to irreversible LPMO oxidative damage and inactivation under redox conditions (25, 45), which could explain the lower activity of the monomer. As both LPMO reactivity and stability are related to H_2O_2 levels (7), we investigated its impact on *Co*AA9A catalysis. Looking at the peroxygenase activity on cellulose of *Co*AA9A in the presence of different H_2O_2 concentrations, we found that low concentrations of H_2O_2 boosted both the monomer and dimer activities (*SI Appendix*, Fig. S14), as observed for other LPMOs (25). Also, we found that the dimer had a slightly higher resistance than the monomer to high (≥100 μM) H_2O_2 concentrations (Fig. 4*D*). In control experiments, we also quantified side activities of the LPMO, viz. its ability to reduce O_2 into H_2O_2 in the absence of substrate (i.e., oxidase activity) and its peroxidase activity. At equivalent amounts of catalytic domains, we found that the monomer and the dimer have comparable oxidase (7.3×10^{-3} s^{-1} and 10×10^{-3} s^{-1}, respectively; *SI Appendix*, Fig. S15*A*) and peroxidase rates (4.8×10^{-3} s^{-1} and 5.0×10^{-3} s^{-1}, respectively; *SI Appendix*, Fig. S14*B*). Altogether, these observations indicate that a stronger binding to cellulose is the main feature driving the higher activity/stability of the dimer.

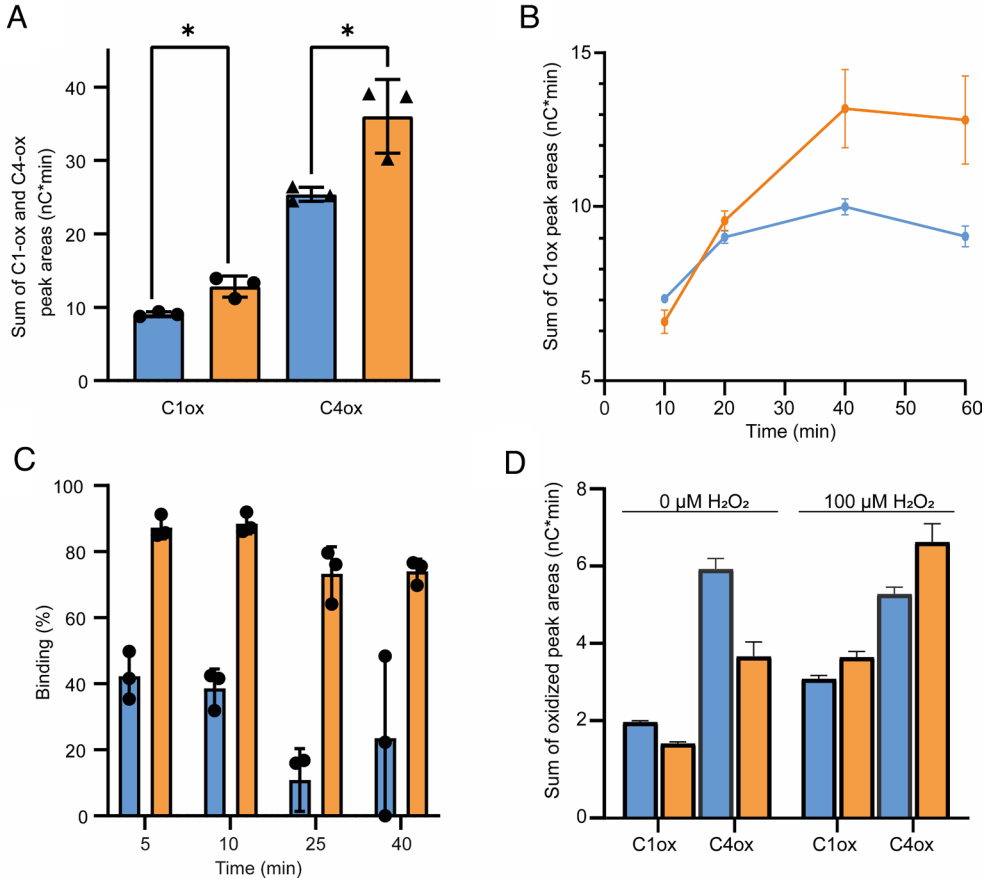

Fig. 4. Impact of the dimerization of *Co*AA9A on cellulose binding and activity. (*A*) Release of C1 and C4 oxidized products after 1 h of incubation with cellulose (0.2% w/v) and ascorbic acid (1 mM) by *Co*AA9A monomer (blue) or dimer (orange) at 2 μM concentration. Asterisks correspond to a *P* value < 0.05. (*B*) Time course release of C1ox products from cellulose during incubation with monomer or dimer (as in panel *A*). (*C*) In vitro binding assays of *Co*AA9A monomer and dimer to PASC (0.2% w/v). Enzymes (5 μM) were incubated from 5 to 40 min at room temperature with cellulose in the presence of ascorbic acid (1 mM). The supernatants, containing the unbound proteins were collected by centrifugation and analyzed by SDS-PAGE. (*D*) Release of C1 and C4 oxidized products after 5 min of incubation with PASC (0.2% w/v) and ascorbic acid (100 μM) by *Co*AA9A monomer or dimer (2 μM) in the absence or presence of 100 μM H_2O_2.

***Co*AA9A Plays a Role in Appressorium Development and Infection.** To investigate the role of *Co*AA9A in plant pathogenesis, we analyzed the expression pattern of *Co*AA9s during the different stages of plant infection (Fig. 5*A*). Interestingly, we found that *Co*AA9A- and *Co*AA9B-encoding genes (TDZ22550 and TDZ14194, respectively) are up-regulated 16 and 12 times at the appressorium stage (4 hours post inoculation, hpi) compared to the initial stage (Fig. 5*B*). We then investigated by western blotting whether *Co*AA9A was secreted at the appressorium stage (Fig. 5*C*). After collection of the extracellular fluid (EF) from the *C. orbiculare* WT strain grown on an artificial inductive surface, we found, consistently with the transcriptomic analysis (Fig. 5*B*), that *Co*AA9A is secreted after 4 h and is barely, if at any extent, detectable after 12 h. Strikingly, only the band corresponding to *Co*AA9A dimer was detected by western blot, suggesting that *Co*AA9A is secreted as a dimer in vivo. The possibility that the antibody used in these experiments might not recognize the monomeric form was checked and ruled out using the recombinant protein (*SI Appendix*, Fig. S16). As a control, the single gene deletion mutant of *C. orbiculare* (Δaa9a) showed the absence of protein. To explore the role of *Co*AA9A in appressorium formation, we followed the early stage of appressorium development at 4 hpi and we found that the Δaa9a strain had a significantly lower frequency of ungerminated conidia and higher frequency of immature appressoria compared to the WT strain (Fig. 5*D*). Furthermore, the Δaa9a strain showed 17 ± 4% lower rate of penetration hyphal formation than the WT at 72 hpi. Introducing *Co*AA9A into the Δaa9a strain restored proper morphogenesis of appressorium and penetration into the host (Fig. 5*E*). Thus, the Δaa9a is functionally complemented by *Co*AA9A. Altogether, our results suggest that *Co*AA9A disruption affects appressorium-mediated plant invasion.

AA9-dCTRs Bearing a Cys Are Widespread among Plant Pathogens. To assess whether the properties of *Co*AA9A are encountered beyond *C. orbiculare*, we analyzed the occurrence of AA9s bearing a Cys before the X283 motif in other fungal phytopathogens (Fig. 6). Interestingly, we found that in almost all the model species analyzed, there was at least one sequence encoding an AA9-X283 with a Cys residue within the dCTR and when transcriptomic data were available, the corresponding genes were up-regulated during plant infection. To assess whether the dimerization was also occurring in some of these species, we successfully heterologously expressed two AA9-X283 (*Ch*AA9A and *Ch*AA9B) from the cereal pathogen *Colletotrichum higginsianum*. We found that *Ch*AA9A and *Ch*AA9B are both able to dimerize and are active against cellulose with a C1/C4 regioselectivity (*SI Appendix*, Figs. S17–S19). SEC-SAXS data confirmed the persistence of disorder in both monomer and dimer forms of *Ch*AA9A and *Ch*AA9B (*SI Appendix*, Figs. S17 and S18). Finally, transcriptomic data available from the literature (47–49) show that these genes are also up-regulated (fold change values > 2) during plant infection (Fig. 6). These data suggest that AA9-dCTRs able to dimerize may be widespread among phytopathogens.

Discussion

To date, LPMOs have mainly been studied for their role in biomass degradation and most functional studies have focused on their catalytic domain, overlooking the potential importance of dCTRs, the preponderance of which was recently unveiled (28). Here, we set off to unravel the biological function of LPMO dCTRs by studying *C. orbiculare*, a well-known model, pathogenic fungus that secretes an array of CAZymes during plant infection, including AA9 LPMOs (36, 46). AA9 LPMOs from *C. orbiculare* are remarkably rich in dCTRs (in ca. 50% of them), and AA9-dCTRs can also be found in other appressorium-forming organisms. Intriguingly, we observed that some of these dCTRs harbor a conserved SLiM (X283 in CAZy), with a positively charged tail that attracted our attention.

Using a combination of protein biochemistry, biophysics, and immunochemistry, we have first made the unexpected observation that the dCTR mediates *Co*AA9A dimerization and confirmed that this dimer is also found in vivo, being secreted by appressoria cells. Mutagenesis allowed us to pinpoint the involvement of a single cysteine, preceding the X283 motif, in the formation of a disulfide bridge mediating dimerization. This LPMO covalent dimer could be regarded as a kind of multimodular LPMO. Multimodularity in LPMOs usually provides beneficial effects, such as increased binding to substrates, increased protein stability and localized substrate oxidation (26). Here, we propose that the dCTR-mediated dimerization of *Co*AA9A creates a flexible spacer allowing to keep the catalytic domain of each monomer apart, thus preserving their individual motions, while, and at the same time, promoting a stronger binding to cellulose. As observed for several LPMOs bearing a CBM (50–52), this stronger binding positively affects the activity of the enzyme, providing notably an enhanced resistance to H_2O_2. Recent works also suggest that domain interactions (in solution) may protect the catalytic domain from oxidative inactivation (53). In line with these observations, we show that both *Co*AA9A C266A and ΔX283 variants exhibit faster enzyme inactivation compared to *Co*AA9A monomer, suggesting that a functional dCTR is needed for optimal enzyme–substrate interactions.

LPMO biological functions only start to be unveiled (9). A few recent reports have notably pinpointed the involvement of LPMOs in the mechanism of a couple of fungal pathogens, notably in *Cryptococcus neoformans* and *Magnaporthe oryzae* (15, 54, 55). Herein, considering that i) *Co*AA9A is a cellulolytic LPMO, ii) *Co*AA9A is secreted as a dimer during appressorium development, and iii) Δaa9a deletion strains displayed impaired penetration capabilities during infection, we hypothesize that *Co*AA9A facilitates plant cell wall disruption during the formation of the penetration hyphae. The dimerization could be an advantage for this LPMO to better control and localize the enzymatic activity. Our results are strengthened by the evidence that dimerization is not unique to *Co*AA9A, being observed also in other AA9 LPMOs, i.e., *Co*AA9B, *Ch*AA9A, and *Ch*AA9B. Importantly, we found that the Cys residue located in the dCTR of AA9-X283s is conserved across most model plant pathogens. This raises the possibility that equivalent dimerization mechanisms may operate in other fungal pathogens and may not be limited to appressorium-forming fungi. We suggest that the absence of a strong phenotype on leaves could be explained by the presence of many other important effectors, including other LPMOs and CAZymes that could compensate the absence of *Co*AA9A. Indeed, we showed that other AA9 LPMO-encoding genes are up-regulated together with *Coaa9a* at early stages, but further experimental work is needed to elucidate their role. The involvement of AA9 LPMOs in plant pathogenesis was recently investigated in *M. oryzae* (54) with a focus on a different AA9 LPMO that cleaves β-1,3 glucans and harbor a chitin-binding domain at its C terminus (15). Of note, *C. orbiculare* and *M. oryzae* share a conserved set of AA9s with similar architecture (40), but the reasons for LPMO genes multiplicity in these plant pathogens and others (both fungi and oomycetes) are still unknown. While it could be related to functional adaptations to different hosts with different strategies to deconstruct plant cell walls (48), it could also be attributed to divergent functions related to their dCTRs.

In conclusion, our study shows that dCTRs in LPMOs are functional and play a key role in modulating the enzyme activity

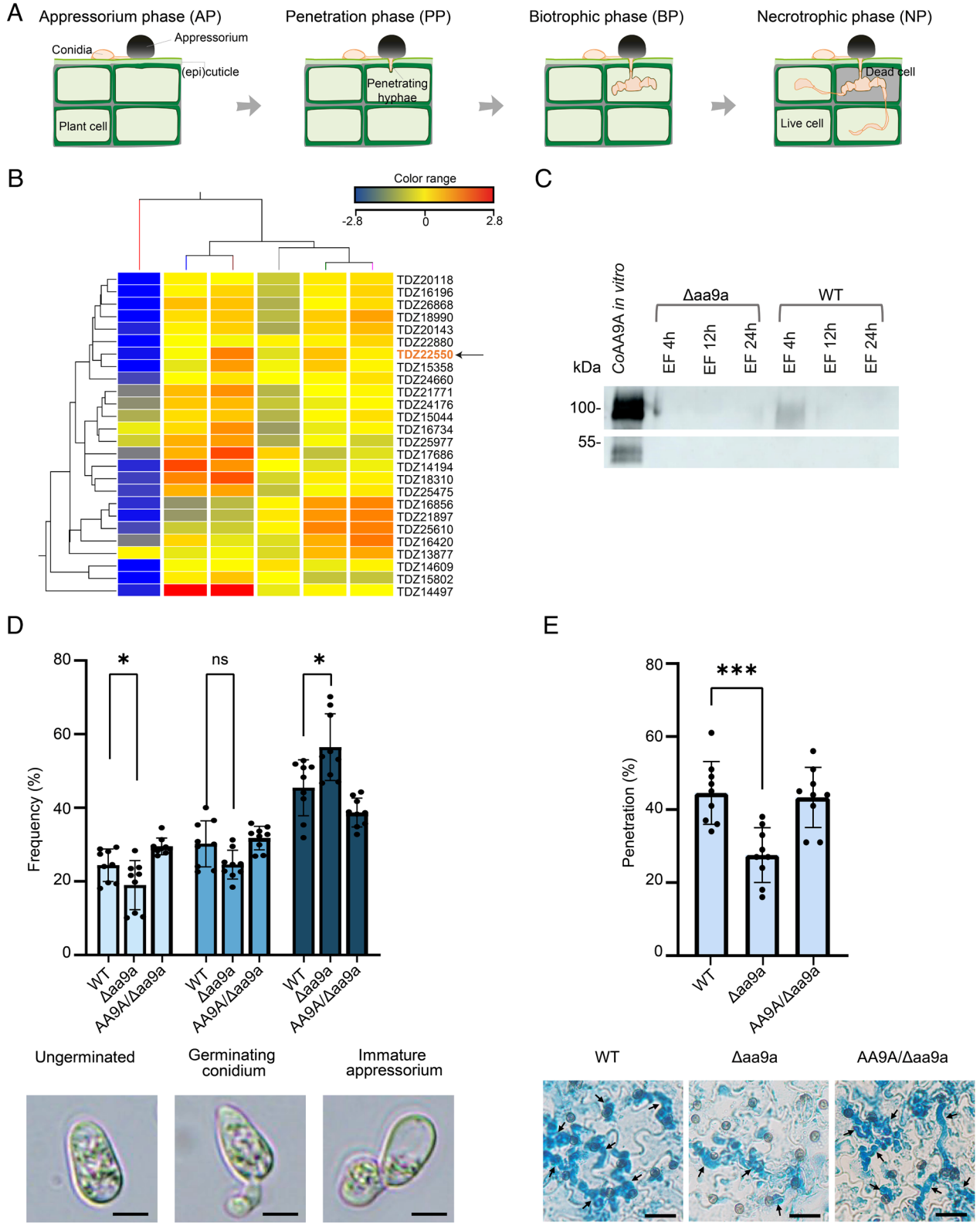

Fig. 5. Role of *Co*AA9A LPMO in vivo during plant infection. (*A*) Multistage plant infection process of appressorium-forming fungi: appressorium (AP), penetration (PP), biotrophic (BP), and necrotrophic (NP) phases. Adapted from ref. 36. (*B*) Transcriptomic analysis of *Co*AA9s during plant infection. Hierarchical clustering was used to visualize gene expression in the wild-type 104-T at 0 h, 2 h, 4 h, 12 h, 24 h, and 48 h after inoculation on cucumber leaves. Transcriptomic data were retrieved from previous datasets (36, 46). The columns were clustered by Euclidean distance. The $\log_2$-transformed expression values per gene were median-normalized. Induced differential expression of a gene is indicated by red, and repressed by blue. *Co*AA9A (TDZ22550) is shown in orange and indicated with a black arrow. (*C*) Western blotting analysis of the EF of *C. orbiculare* WT and Δaa9a strains during appressorium formation on inductive surface. (*D*) Frequency of conidial germination and appressorium development after 4 hpi of *C. orbiculare* WT, Δaa9a, and complementation strain AA9A/Δaa9a. Error bars correspond to SD from three independent biological replicates. At least 300 conidia were observed in each replicate. (Scale bar, 5 μm.) (*E*, *Upper*) Penetrating hyphae formation of *C. orbiculare* WT, Δaa9a, and AA9A/Δaa9a strains at 72 hpi on cucumber cotyledons. Error bars correspond to SD from three independent biological replicates of appressoria that formed penetration hyphae. At least 300 appressoria were analyzed in each replicate. In panels *D* and *E*, a Student's *t* test was applied (ns, not significant, $*P \leq 0.05$, $***P \leq 0.001$). (*Lower*) Appressoria morphology and penetration hyphal development on lower surface of detached cucumber cotyledons at 3 d post inoculation. Penetration hyphae were stained with lactophenol aniline blue. Arrows indicate penetration hyphae. (Scale bar, 20 μm.)

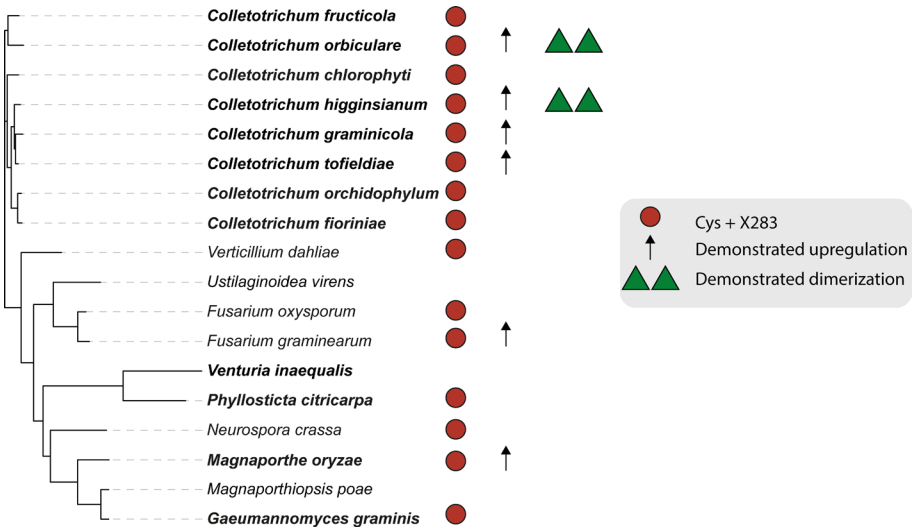

Fig. 6. Occurrence and regulation of the AA9-X283 LPMOs among fungal phytopathogens. Phylogenetic tree adapted from ref. 36. Red circles indicate the species' genomes encoding for at least one AA9 where the X283 motif is preceded by a Cys. When transcriptomic data were available, upregulation was observed during plant infection (indicated by black arrows). Green triangles indicate dimerization of *Co*AA9A, *Co*AA9B, *Ch*AA9A, and *Ch*AA9B, as demonstrated in this study (see *SI Appendix*, Figs. S17 and S18 for *Ch*AA9s). Bold lettering indicates species that form melanized appressorium/hyphopodia.

and plant pathogenesis. We think that considering these hitherto overlooked dCTRs is crucial to get an accurate understanding of LPMOs biochemistry and decipher their mode of action in biological systems. We anticipate that their importance may extend to other biological contexts.

Materials and Methods

Bioinformatic Analysis. To analyze the C-terminal regions of *C. orbiculare*, we retrieved all the AA9 sequences available in the JGI Mycocosm and then analyzed unannotated C-terminal regions with IUPred2A. A residue was considered disordered if IUPred2A returned a value equal or higher than 0.5. A region was considered as a dCTR if it had at least 20 consecutive residues predicted to be disordered. Charge patterning in each dCTR was analyzed by computing the κ parameter with localCIDER (56).

To build the phylogenetic tree of AA9s, we retrieved 24 AA9-X283 sequences from *Colletotrichum* species available in JGI Mycocosm (40). The variable C-terminal extensions were manually removed in order to keep only the catalytic domains. The AA9 sequences were aligned using MCoffee, which combines several alignment methods (57). The resulting multiple sequence alignments were used to infer the phylogenetic trees via the IQ-tree webserver (58). The Whelan and Goldman amino acid substitution model with a gamma distribution containing four rate categories (G4) has been identified as the best-fitting model based on the Bayesian information criterion. Branch support was calculated by 1,000 bootstraps alignments using the ultrafast bootstrap analysis method.

Generation of Structural Models. *Co*AA9A and *Co*AA9B monomer structural models were generated using AlphaFold2 Colab notebook (41, 59), while the *Co*AA9A dimer structural model was generated using AlphaFold-Multimer in ChimeraX (60, 61).

Heterologous Protein Production. The proteins were produced using the in-house 3PE platform (*P. pastoris* Protein Express; www.platform3pe.com/) as described in ref. 62. The nucleotide sequence coding for the AA9A and AA9B of *C. orbiculare* (Genbank ID TDZ22550, TDZ14194, respectively), and the sequences encoding *Co*AA9A C266A and ΔX283, and *Ch*AA9A and *Ch*AA9B of *C. higginsianum* (Genbank ID XP_018155356.1, XP_018155797.1, respectively) were codon optimized and synthesized (GenScript, Piscataway) for expression in *P. pastoris* (syn. *Komagataella phaffii*). Each gene was inserted into the expression vector pPICZαA (Invitrogen, Cergy-Pontoise, France). PmeI-linearized pPICZαA recombinant plasmids were used to transform by electroporation competent *P. pastoris* SuperMan5 cells (*Co*AA9A WT and mutants and *Co*AA9B) and X33 cells (*Ch*AA9A and *Ch*AA9B). The best-producing transformants were grown in 2 L flasks as described previously (62). The medium was supplemented, initially and every day, with 0.5% (v/v) methanol for *Co*AA9A WT and mutants or 3% (v/v) methanol for *Co*AA9B, *Ch*AA9A, and *Ch*AA9B, respectively, at 20 °C in an orbital shaker (200 rpm) for another 3 d. The cells were harvested by centrifugation (5,000 rpm, 10 min at 4 °C), and just before purification the pH of the supernatant was adjusted to eight with sodium hydroxide. The supernatant was then filtered using 0.45-μm filters (Millipore, Burlington, MA).

Protein Purification. Filtered and pH-adjusted culture supernatants were loaded onto a HiPrep 26/10 Desalting column (Cytiva, Velizy-Villacoublay, France), equilibrated with buffer A (Tris-HCl 50 mM pH 8, NaCl 10 mM), that was connected to an Äkta pure 100 (Cytiva). Fractions containing the proteins were pooled and loaded onto a 20-mL HiPrep DEAE FF 16/10 and recombinant proteins were eluted with buffer B (Tris-HCl 50 mM pH 8, NaCl 1M). Fractions containing recombinant enzymes were pooled, concentrated, and purified by SEC, using a HiLoad 16/600 Superdex 75-pg column (Cytiva) operated at 1 mL min^{-1} with MES 50 mM NaCl 150 mM, pH 6.5 as elution buffer. The protein concentrations were determined by absorption at 280 nm using a Nanodrop ND-2000 spectrophotometer (Thermo Fisher Scientific, Waltham, MA) and extinction coefficient (*Co*AA9A: 51,590 M^{-1} cm^{-1}, C266A: 51,590 M^{-1} cm^{-1}, ΔX283: 50,100 M^{-1} cm^{-1}, *Co*AA9B: 47,120 M^{-1} cm^{-1}, *Ch*AA9A: 53,985 M^{-1} cm^{-1}, *Ch*AA9B: 49,640 M^{-1} cm^{-1}) determined with ProtParam (Expasy). Protein purity was checked by SDS-PAGE using a 4 to 20% Tris-glycine precast gel (BioRad, Gemenos, France), followed by Coomassie Blue staining.

Thermal Shift Assay. Determination of Tm(app) was made using a protein thermal shift assay (Thermo Fisher Scientific). The assay monitors protein unfolding using the fluorescent dye SYPRO Orange. SYPRO Orange 5,000× was diluted to 5× in buffer MES 50 mM, NaCl 150 mM, pH 6.5 and mixed with 10 μM of *Co*AA9A monomer, dimer, or variants. Reactions were heated from 25 to 99 °C in 96-well plates over the course of 60 min in a CFX Connect real-time PCR machine (Bio-Rad, Hercules, CA). The fluorescence was measured using as excitation and emission wavelengths at 485 nm and 625 nm, respectively. The experiments were performed in three replicates.

ICP-MS. Copper content was analyzed using ICP-MS as described in ref. 63. The *Co*AA9A monomer or dimer was mineralized, then diluted in ultrapure water, and analyzed by an ICAP Q apparatus (Thermo Electron, Les Ullis, France). The copper concentration was determined using Plasmalab (Thermo Electron) software, at m/z = 63 with an accuracy of ±5%.

SEC-MALLS. The molecular mass was calculated using analytical SEC coupled with online MALLS, ultra-violet light absorbance, and refractive index detectors (Wyatt Technology). SEC was performed on a Superdex200 10/300 GL Increase column with 50 mM MES pH 6.5, 150 mM NaCl as the elution buffer. The molecular mass was calculated using ASTRA V software (Wyatt Technology) with a refractive index increment (dn/dc) of 0.185 mL g^{-1} for protein samples. In the "protein conjugate" analysis, the refractive index increment of glycans was set to 0.136 mL g^{-1}.

Protein N-Deglycosylation. *Co*AA9A monomer, dimer, C266A and ΔX283, variants were treated with 50 mU of Endoglycosidase H (EndoH; REF: 11643053001, Roche) per mg of protein in MES 50 mM, NaCl 150 mM pH 6.5. The mixture was incubated overnight, at room temperature, with gentle mixing. EndoH was

removed by injecting the sample onto a Superdex 200 10/300 GL with MES 50 mM NaCl 150 mM, pH 6.5 as elution buffer. Fractions containing the deglycosylated proteins were pooled and concentrated up to the final concentrations used for SEC-SAXS reported in *SI Appendix*, Table S2.

SAXS. SEC-SAXS data were collected at the European Synchrotron Radiation Facility (ESRF, Grenoble, France) and at SOLEIL (Gif-sur-Yvette, France) as described in *SI Appendix*, Table S2.

Data reductions were performed using the established procedure available at BM29 beamline or using the software FOXTROT according to the SWING beamline procedure. Buffer background runs were subtracted from sample runs using CHROMIX in the ATSAS program package (64). The final scattering intensities were analyzed using the ATSAS program package. Linearity in the Guinier region was used to exclude sample aggregation. The few data points differing from the Guinier fitting at low angles were deleted and the useful data range was determined with SHANUM (65). The radius of gyration (R_g) was estimated at low angles (with $q < 1.3/R_g$ as an upper limit) (*SI Appendix*, Table S3) according to the Guinier approximation (66, 67):

$$ln\, I(q) = ln\, I_0 - \frac{(q^2 R_g^2)}{3}.$$

The pairwise distance distribution function, P(r), from which the Dmax and the R_g were estimated, was computed using GNOM and manually adjusted until a good CorMap *P*-value ($\alpha > 0.01$) was obtained (68). The theoretical R_g value (in Å) expected for various conformational states was calculated using the Flory equation

$$R_g = R_0 N^{\nu},$$

where N is the number of amino acid residues, R_0 a constant and ν a scaling factor. For IDPs, R_0 is 2.54 ± 0.01 and ν is 0.522 ± 0.01 (69), for chemically denatured (U) proteins R_0 is 1.927 ± 0.27 and ν is 0.598 ± 0.028 (69), and for natively folded (NF) proteins $R_0 = \sqrt{(3/5)} \times 4.75$ and $\nu = 0.29$ (70). The flexibility of the proteins was assessed with the dimensionless Kratky plot [$(qR_g)^2\, I(q)/I_0$ vs. qR_g].

Modeling of the *Co*AA9A dimer as conformational ensembles was done with the program suite EOM 2.1 (71) using default parameters. EOM first generates an initial pool of 10,000 random, Cα-only conformers from the amino acid sequence. Subsequently, from this pool EOM 2.1 generates a conformational sub-ensemble that best fits the experimental SAXS data. To minimize over-fitting, EOM attempts at minimizing the number of conformers able to fit the experimental data and usually generates ensembles consisting of 5 to 40 conformers. The amino acid sequence provided as input to EOM was that of the recombinant protein without the signal peptide. The two catalytic domains were modeled with AlphaFold2 (41) and assigned as structured domains, while the dCTRs were kept unstructured and the distance between the C266 in each monomer was set between 5 and 6 Å. Gaussian distributions of R_g and D_{max} of the generated conformers were automatically calculated as well as their respective theoretical scattering profile and fit to the experimental data. EOM uses a genetic algorithm to select an ensemble that best fits the experimental scattering curve. From the width of the R_g distribution the flexibility of the particles can be extracted, whereby a narrow distribution indicates a rather rigid particle and broader distributions indicate higher flexibility. Using EOM 2.1, systematic quantification of the flexibility was made using the metric Rflex, which computes the Shannon information entropy of the distributions (71).

The low-resolution shape of the *Co*AA9A dimer was determined ab initio from the scattering curve using the program GASBOR (43). This program restores low-resolution shapes of protein and calculates a volume filled with densely packed spheres (dummy residues) fitting the experimental scattering curve by a simulated annealing minimization procedure and considering the protein as an assembly of dummy residues centered on the Cα positions (spheres of 3.8 Å diameter) with a nearest-neighbor distribution constraint. Several independent fits were run with no symmetry restriction with an input of 600 dummy residues, corresponding to ~70-kDa protein.

Enzyme Assays. Activity on phosphoric acid swollen cellulose (PASC) at a concentration of 2 mg mL^{-1} (eq. 0.2% w/v) was measured in a 100 µL reaction mixture containing *Co*AA9A monomer, dimer, or variants (at 2 µM), in MES buffer (50 mM, pH 6.5) or *Co*AA9B, *Ch*AA9A, *Ch*AA9B (1 µM) in sodium acetate buffer (50 mM pH 5.2). Reactions were supplemented with ascorbic acid (1 mM) or *Pa*CDHB (2 µM) and incubated at 30 °C, with shaking at 850 rpm. Reactions were stopped by adding 100 µL NaOH 0.2 M, and then centrifuged before being diluted (1:2) in water for analysis of the soluble fraction using a high-performance anion-exchange chromatography coupled with pulsed amperometric detection (DIONEX ICS6000 system, Thermo Fisher Scientific) equipped with a CarboPac-PA1 guard column (2 × 50 mm) and a CarboPac-PA1 column (2 × 250 mm). Elution was carried out at a flow rate of 0.25 mL min^{-1} and 25 µL of sample was injected. The solvents used were 100 mM NaOH (eluent A) and NaAc (1 M) in 100 mM NaOH (eluent B), and the following gradient was applied: 0 to 10 min, 0 to 10% B; 10 to 35 min, 10 to 35% B (linear gradient); 35 to 40 min, 30 to 100% B (curve 6); 40 to 41 min, 100 to 0% B; 41 to 50 min, 100% A. Integration was performed using Chromeleon 7.2.10 software.

Oxidase and Peroxidase Production Assays. Production of H_2O_2 (oxidase activity) was quantified using the Amplex Red assay (72). Reaction mixtures contained 2 µM *Co*AA9A variants, 100 µM Amplex Red (Thermo Fisher Scientific), 0.1 mg mL^{-1} horseradish peroxidase (Sigma-Aldrich), in 10 mM sodium phosphate, pH 7.0, and were incubated at 23 °C. The reactions were initiated by adding ascorbic acid (50 µM) and the formation of resorufin was followed spectrophotometrically at 575 nm. A control reaction without *Co*AA9A variants was carried out in parallel and a standard curve of H_2O_2 was performed under the same conditions.

Consumption of H_2O_2 (peroxidase reaction) was measured using the protocol described by Breslmayr et al. (73). This assay is based on the oxidation of 2,6-dimethoxyphenol (DMP) to coerulignone by the enzyme in the presence of H_2O_2. Reaction mixtures contained 2 µM *Co*AA9A variants, 500 µM 2,6-DMP, and 100 µM H_2O_2 in 50 mM phosphate buffer, pH 7. Reactions were initiated by addition of DMP and the release of coerulignone was monitored at 469 nm in a plate reader (ε_{469} = 53,200 M^{-1} cm^{-1}). Control reactions without *Co*AA9A variants were performed in parallel.

Cellulose Binding Assays. The binding affinity of *Co*AA9A (5 µM) for PASC (1%) was monitored by measuring the concentration of the protein in the supernatant after 5, 10, 25, or 40 min of incubation in a Thermomixer (Eppendorf, Hamburg, Germany) (30 °C, 850 rpm). For each condition, a control reaction in the absence of substrate was carried out. The protein concentration in the unbound fraction was measured by SDS-PAGE in non-reducing conditions. All the reactions were performed at pH 6.5 (50 mM MES buffer) and repeated three times. A calibration curve with known and increasing amounts of protein loaded on an SDS-PAGE gel was used to determine the percentage of binding.

***C. orbiculare* Strain Construction.** *C. orbiculare* strain 104-T (MAFF240422) was used as the wild-type strain. All strains used in this study (*SI Appendix*, Table S4) were cultured at 24 °C on 3.9% potato dextrose agar (PDA; Nissui, Japan). *C. orbiculare* was transformed using *Agrobacterium tumefaciens* C58C1 as previously described (37, 74). For genetic manipulation, *Escherichia coli* DH5α-competent cells were maintained at 37 °C on Luria-Bertani agar. For generating the *Co*AA9A disruption mutant, the 1.4-kb upstream and 1.1-kb downstream flanking sequences and a 1.4-kb hygromycin-resistance gene cassette were amplified and introduced into linearized binary vector pPZP-PvuII using the In-Fusion HD Cloning kit (TaKaRa Bio USA, Inc.). Gene deletion of mutants was confirmed by genomic PCR analysis using the two primer pairs listed in *SI Appendix*, Table S4. For constructing AA9A gene complementation vector, AA9A gene fragments containing the 1.4-kb upstream and 1.1-kb downstream flanking sequences were inserted into the linearized pPZP-SUR. The primers and plasmids used in this study are listed in *SI Appendix*, Table S5.

Infection Structure Differentiation. For observation of conidial germination and appressorium formation of *C. orbiculare*, a conidial suspension (5 × 10^5 conidia mL^{-1} in distilled water) was placed on a multi-well glass slide (Matsunami Glass, Japan) and incubated in a humid box at 24 °C in the dark for 4 h. For observation of penetration hyphae, cucumber cotyledons were inoculated in a humid box with 5 × 10^5 conidia mL^{-1}, incubated at 24 °C for 72 h, and then stained with 0.1% (w/v) lactophenol aniline blue solution as previously described (75). Bright-field microscopic images were acquired using a Nikon ECLIPSE E600 microscope equipped with a 40× water immersion lens (Nikon, Japan) and an OLYMPUS DP74 digital camera system (Olympus, Japan).

Production of Antibodies, Protein Electrophoresis, and Immunoblotting. A solution of 3 mg of purified recombinant, monomeric *Co*AA9A protein was used to elicit rabbit polyclonal antibodies according to the manufacturer's procedure

(Biotem). For appressorium formation in vitro, conidia of *C. orbiculare* were harvested from PDA cultures incubated for 5 d. A conidial suspension (5×10^5 conidia mL^{-1} in distilled water) was placed on a polystyrene petri dish or a multi-well glass slide (Matsunami Glass) and incubated in a humid box at 24 °C. Total secreted proteins were collected by centrifugation (11,000 g, 20 min, 4 °C). Protein analyses were carried out by using 4 to 20% Mini-Protean TGX precast protein stain-free gels in a Mini-Protean electrophoresis cell system (both Bio-Rad). Specificity of the antibodies was determined by immunoblot of total protein obtained from the EF of appressorium formation using the Clarity Western ECL Substrate (Bio-Rad Laboratories) according to the manufacturer's instructions.

Data, Materials, and Software Availability. Sequence data in this study can be found in the GenBank/EMBL database under the indicated accession numbers: *C. orbiculare Co*AA9A (TDZ22550) (76), *Co*AA9B (TDZ14194) (77), *Co*AA9s (TDZ20118 (78), TDZ16196 (79), TDZ26868 (80), TDZ18990 (81), TDZ20143 (82), TDZ22880 (83), TDZ15358 (84), TDZ24660 (85), TDZ21771 (86), TDZ24176 (87), TDZ15044 (88), TDZ16734 (89), TDZ25977 (90), TDZ17686 (91), TDZ18310 (92), TDZ25475 (93), TDZ16856 (94), TDZ21897 (95), TDZ25610 (96), TDZ16420 (97), TDZ13877 (98), TDZ14609 (99), TDZ15802 (100), TDZ14497 (101)), *C. higginsianum Ch*AA9A (XP_018155356.1) (102), and *Ch*AA9B (XP_018155797.1) (103). SEC-SAXS data have been deposited in the Small-Angle Scattering Biological Data Bank (SASBDB, https://www.sasbdb.org/) (104) under the following codes: SASDUG3 (105): C. *orbiculare* AA9A LPMO monomer; SASDUH3 (106): C. *orbiculare* AA9A LPMO dimer; SASDUJ3 (107): C. *orbiculare* AA9A LPMO ΔX283; SASDUK3 (108): C. *orbiculare* AA9A LPMO C266A; SASDUL3 (109): C. *higginsianum* AA9A LPMO monomer; SASDUM3 (110): C. *higginsianum* AA9A LPMO dimer; SASDUN3 (111): C. *higginsianum* AA9B LPMO monomer; SASDUP3 (112): C. *higginsianum* AA9B LPMO dimer. The conformational ensemble of CoAA9A derived using SEC-SAXS data has been deposited within the Protein Ensemble Database (PED-DB, https://proteinensemble.org/) (113) under accession number PED00506 (114).

ACKNOWLEDGMENTS. This work was partly supported by the French Infrastructure for Integrated Structural Biology (ANR-10-INSB- 0005). K.C.T. fellowship was funded by the French government under the France 2030 investment plan, as part of the Initiative d'Excellence d'Aix-Marseille Université–A*MIDEX and is part of the Institute of Microbiology, Bioenergies and Biotechnology–IM2B (AMX-19-IET-006). Work in Japan was supported by the Japan Society for the Promotion of Science Grants-in-Aid for Scientific Research–KAKENHI, grant numbers 20H02989 to Y.K., and 20K15529, 23K13956 to S.K. We thank the NovoNordisk foundation (OxyMiST project, grant number NNF20OC0059697) for funding. Part of the work described was performed using services provided by the 3PE platform, a member of IBISBA-FR (https://doi.org/10.15454/08BX-VJ91; www.ibisba.fr), the French node of the European research infrastructure, EU-IBISBA (www.ibisba.eu). We thank Florence Chaspoul Institut Méditerranéen de Biodiversité et d'Ecologie (IMBE) for ICP-MS analysis, Aurélien Thureau (SOLEIL), A. Popov and E. Foldesne Dudas (ESRF) for their help in recording SEC-SAXS data, ESRF and the SOLEIL synchrotrons for beamtime allocation. We are also grateful to Gerlind Sulzenbacher (AFMB lab) for efficiently managing the AFMB BAG and Maté Perez for help with SEC-MALLS analyses done using the Marseille Integrative Structural Biology facility (https://www.afmb.univ-mrs.fr/en/facility/structural-biology/) supported by Infrastructures Biologie Santé et Agronomie and Plateforme Technologique Aix-Marseille. We thank all the AFMB technical and support staff (Denis Patrat, Patricia Clamecy, Béatrice Rolland, Paul Zamboni, Chantal Falaschi, and Fabienne Amalfitano).

Author affiliations: [a]CNRS Aix Marseille Université, CNRS, Architecture et Fonction des Macromolécules Biologiques, UMR 7257, Marseille 13009, France; [b]Institut National de la Recherche pour l'Agriculture, l'Alimentation et l'Environnement, Biodiversité et Biotechnologie Fongiques, UMR 1163, Aix Marseille Université, Marseille 13009, France; [c]Faculty of Agriculture, Setsunan University, Osaka 573-0101, Japan; [d]Institut National de la Recherche pour l'Agriculture, l'Alimentation et l'Environnement, Aix Marseille Université, 3PE Platform, Marseille 13009, France; and [e]Division of Functional Genomics, Advanced Science Research Center, Kanazawa University, Kanazawa 920-1164, Japan

1. R. J. Quinlan *et al.*, Insights into the oxidative degradation of cellulose by a copper metalloenzyme that exploits biomass components. *Proc. Natl. Acad. Sci. U.S.A.* **108**, 15079–15084 (2011).
2. G. Vaaje-Kolstad *et al.*, An oxidative enzyme boosting the enzymatic conversion of recalcitrant polysaccharides. *Science* **330**, 219–222 (2010).
3. B. Bissaro, A. Várnai, Å. K. Røhr, V. G. H. Eijsink, Oxidoreductases and reactive oxygen species in conversion of lignocellulosic biomass. *Microbiol. Mol. Biol. Rev.* **82**, e00029-18 (2018).
4. Z. Forsberg *et al.*, Cleavage of cellulose by a CBM33 protein. *Protein Sci. Publ. Protein Soc.* **20**, 1479–1483 (2011).
5. C. M. Phillips, W. T. Beeson, J. H. Cate, M. A. Marletta, Cellobiose dehydrogenase and a copper-dependent polysaccharide monooxygenase potentiate cellulose degradation by *Neurospora crassa*. *ACS Chem. Biol.* **6**, 1399–1406 (2011).
6. A. Villares *et al.*, Lytic polysaccharide monooxygenases disrupt the cellulose fibers structure. *Sci. Rep.* **7**, 40262 (2017).
7. B. Bissaro, V. G. H. Eijsink, Lytic polysaccharide monooxygenases: Enzymes for controlled and site-specific Fenton-like chemistry. *Essays Biochem.* **67**, 575–584 (2023).
8. K. S. Johansen, Discovery and industrial applications of lytic polysaccharide mono-oxygenases. *Biochem. Soc. Trans.* **44**, 143–149 (2016).
9. T. M. Vandhana *et al.*, On the expansion of biological functions of lytic polysaccharide monooxygenases. *New Phytol.* **233**, 2380–2396 (2022).
10. M. Qu *et al.*, AA15 lytic polysaccharide monooxygenase is required for efficient chitinous cuticle turnover during insect molting. *Commun. Biol.* **5**, 1–12 (2022).
11. R. A. Yao *et al.*, The *Ustilago maydis* AA10 LPMO is active on fungal cell wall chitin. *Appl. Environ. Microbiol.* **89**, e0057323 (2023).
12. F. Askarian *et al.*, Immunization with lytic polysaccharide monooxygenase CbpD induces protective immunity against *Pseudomonas aeruginosa* pneumonia. *Proc. Natl. Acad. Sci. U.S.A.* **120**, e2301538120 (2023).
13. E. Chiu *et al.*, Structural basis for the enhancement of virulence by viral spindles and their in vivo crystallization. *Proc. Natl. Acad. Sci. U.S.A.* **112**, 3973–3978 (2015).
14. F. Sabbadin *et al.*, Secreted pectin monooxygenases drive plant infection by pathogenic oomycetes. *Science* **373**, 774–779 (2021).
15. A. Martinez-D'Alto, *et al.*, Characterization of a unique polysaccharide monooxygenase from the plant pathogen *Magnaporthe oryzae*. *Proc. Natl. Acad. Sci. U.S.A.* **120**, e2215426120 (2023).
16. E. Drula *et al.*, The carbohydrate-active enzyme database: Functions and literature. *Nucleic Acids Res.* **50**, D571–D577 (2022).
17. R. Berlemont, Distribution and diversity of enzymes for polysaccharide degradation in fungi. *Sci. Rep.* **7**, 222 (2017).
18. J. W. Agger *et al.*, Discovery of LPMO activity on hemicelluloses shows the importance of oxidative processes in plant cell wall degradation. *Proc. Natl. Acad. Sci. U.S.A.* **111**, 6287–6292 (2014).
19. C. Bennati-Granier *et al.*, Substrate specificity and regioselectivity of fungal AA9 lytic polysaccharide monooxygenases secreted by *Podospora anserina*. *Biotechnol. Biofuels* **8**, 90 (2015).
20. T. Isaksen *et al.*, A C4-oxidizing lytic polysaccharide monooxygenase cleaving both cellulose and cello-oligosaccharides. *J. Biol. Chem.* **289**, 2632–2642 (2014).
21. K. E. H. Frandsen, L. Lo Leggio, Lytic polysaccharide monooxygenases: A crystallographer's view on a new class of biomass-degrading enzymes. *IUCrJ* **3**, 448–467 (2016).
22. G. Vaaje-Kolstad, Z. Forsberg, J. S. Loose, B. Bissaro, V. G. Eijsink, Structural diversity of lytic polysaccharide monooxygenases. *Curr. Opin. Struct. Biol.* **44**, 67–76 (2017).
23. L. Ciano, G. J. Davies, W. B. Tolman, P. H. Walton, Bracing copper for the catalytic oxidation of C-H bonds. *Nat. Catal.* **1**, 571–577 (2018).
24. D. Kracher *et al.*, Extracellular electron transfer systems fuel cellulose oxidative degradation. *Science* **352**, 1098–1101 (2016).
25. B. Bissaro *et al.*, Oxidative cleavage of polysaccharides by monocopper enzymes depends on H_2O_2. *Nat. Chem. Biol.* **13**, 1123–1128 (2017).
26. Z. Forsberg, G. Courtade, On the impact of carbohydrate-binding modules (CBMs) in lytic polysaccharide monooxygenases (LPMOs). *Essays Biochem.* **67**, 561–574 (2023).
27. N. Lenfant *et al.*, A bioinformatics analysis of 3400 lytic polysaccharide oxidases from family AA9. *Carbohydr. Res.* **448**, 166–174 (2017).
28. K. C. Tamburrini *et al.*, Bioinformatic analysis of lytic polysaccharide monooxygenases reveals the pan-families occurrence of intrinsically disordered C-terminal extensions. *Biomolecules* **11**, 1632 (2021).
29. A. K. Dunker *et al.*, What's in a name? Why these proteins are intrinsically disordered: Why these proteins are intrinsically disordered. *Intrinsically Disord. Proteins* **1**, e24157 (2013).
30. J. Habchi, P. Tompa, S. Longhi, V. N. Uversky, Introducing protein intrinsic disorder. *Chem. Rev.* **114**, 6561–6588 (2014).
31. P. Tompa, Intrinsically unstructured proteins. *Trends Biochem. Sci.* **27**, 527–533 (2002).
32. N. D. Keul *et al.*, The entropic force generated by intrinsically disordered segments tunes protein function. *Nature* **563**, 584–588 (2018).
33. M. Larion, R. K. Salinas, L. Bruschweiler-Li, B. G. Miller, R. Brüschweiler, Order-disorder transitions govern kinetic cooperativity and allostery of monomeric human glucokinase. *PLoS Biol.* **10**, e1001452 (2012).
34. B. Szabo *et al.*, Intrinsically disordered linkers impart processivity on enzymes by spatial confinement of binding domains. *Int. J. Mol. Sci.* **20**, 2119 (2019).
35. R. Dean *et al.*, The Top 10 fungal pathogens in molecular plant pathology. *Mol. Plant Pathol.* **13**, 414–430 (2012).
36. B. Bissaro *et al.*, Tandem metalloenzymes gate plant cell entry by pathogenic fungi. *Sci. Adv.* **8**, eade9982 (2022).
37. S. Kodama *et al.*, The morphogenesis-related NDR kinase pathway of *Colletotrichum orbiculare* is required for translating plant surface signals into infection-related morphogenesis and pathogenesis. *PLOS Pathog.* **13**, e1006189 (2017).
38. B. Mészáros, G. Erdős, Z. Dosztányi, IUPred2A: Context-dependent prediction of protein disorder as a function of redox state and protein binding. *Nucleic Acids Res.* **46**, W329–W337 (2018).
39. N. E. Davey *et al.*, Attributes of short linear motifs. *Mol. Biosyst.* **8**, 268–281 (2012).
40. I. V. Grigoriev *et al.*, MycoCosm portal: Gearing up for 1000 fungal genomes. *Nucleic Acids Res.* **42**, D699–D704 (2014).
41. J. Jumper *et al.*, Highly accurate protein structure prediction with AlphaFold. *Nature* **596**, 583–589 (2021).
42. A. G. Kikhney, D. I. Svergun, A practical guide to small angle X-ray scattering (SAXS) of flexible and intrinsically disordered proteins. *FEBS Lett.* **589**, 2570–2577 (2015).
43. D. I. Svergun, M. V. Petoukhov, M. H. Koch, Determination of domain structure of proteins from X-ray solution scattering. *Biophys. J.* **80**, 2946–2953 (2001).

44. D. Kracher, M. Andlar, P. G. Furtmüller, R. Ludwig, Active-site copper reduction promotes substrate binding of fungal lytic polysaccharide monooxygenase and reduces stability. *J. Biol. Chem.* **293**, 1676–1687 (2018).
45. J. S. M. Loose *et al.*, Multipoint precision binding of substrate protects lytic polysaccharide monooxygenases from self-destructive off-pathway processes. *Biochemistry* **57**, 4114–4124 (2018).
46. F. Fukada, S. Kodama, T. Nishiuchi, N. Kajikawa, Y. Kubo, Plant pathogenic fungi *Colletotrichum* and *Magnaporthe* share a common G1 phase monitoring strategy for proper appressorium development. *New Phytol.* **222**, 1909–1923 (2019).
47. S. Hacquard *et al.*, Survival trade-offs in plant roots during colonization by closely related beneficial and pathogenic fungi. *Nat. Commun.* **7**, 11362 (2016).
48. R. J. O'Connell *et al.*, Lifestyle transitions in plant pathogenic *Colletotrichum* fungi deciphered by genome and transcriptome analyses. *Nat. Genet.* **44**, 1060–1065 (2012).
49. K. D. Puri, C. Yan, Y. Leng, S. Zhong, RNA-Seq revealed differences in transcriptomes between 3ADON and 15ADON populations of *Fusarium graminearum in vitro* and *in planta*. *PLoS One* **11**, e0163803 (2016).
50. A. Chalak *et al.*, Influence of the carbohydrate-binding module on the activity of a fungal AA9 lytic polysaccharide monooxygenase on cellulosic substrates. *Biotechnol. Biofuels* **12**, 206 (2019).
51. G. Courtade, Z. Forsberg, E. B. Heggset, V. G. H. Eijsink, F. L. Aachmann, The carbohydrate-binding module and linker of a modular lytic polysaccharide monooxygenase promote localized cellulose oxidation. *J. Biol. Chem.* **293**, 13006–13015 (2018).
52. Z. Forsberg *et al.*, Structural and functional analysis of a lytic polysaccharide monooxygenase important for efficient utilization of chitin in *Cellvibrio japonicus*. *J. Biol. Chem.* **291**, 7300–7312 (2016).
53. Z. Forsberg *et al.*, The effect of linker conformation on performance and stability of a two-domain lytic polysaccharide monooxygenase. *J. Biol. Chem.* **299**, 105262 (2023).
54. Y. Li *et al.*, Magnaporthe oryzae auxiliary activity protein MoAa91 functions as chitin-binding protein to induce appressorium formation on artificial inductive surfaces and suppress plant immunity. *mBio* **11**, e03304-19 (2020).
55. C. Probst *et al.*, A fungal lytic polysaccharide monooxygenase is required for cell wall integrity, thermotolerance, and virulence of the fungal human pathogen *Cryptococcus neoformans*. *PLoS Pathog.* **19**, e1010946 (2023).
56. A. S. Holehouse, R. K. Das, J. N. Ahad, M. O. G. Richardson, R. V. Pappu, CIDER: Resources to analyze sequence-ensemble relationships of intrinsically disordered proteins. *Biophys. J.* **112**, 16–21 (2017).
57. I. M. Wallace, O. O'Sullivan, D. G. Higgins, C. Notredame, M-Coffee: Combining multiple sequence alignment methods with T-Coffee. *Nucleic Acids Res.* **34**, 1692–1699 (2006).
58. L.-T. Nguyen, H. A. Schmidt, A. von Haeseler, B. Q. Minh, IQ-TREE: A fast and effective stochastic algorithm for estimating maximum-likelihood phylogenies. *Mol. Biol. Evol.* **32**, 268–274 (2015).
59. M. Mirdita *et al.*, ColabFold: Making protein folding accessible to all. *Nat. Methods* **19**, 679–682 (2022).
60. R. Evans *et al.*, Protein complex prediction with AlphaFold-multimer. bioRxiv [Preprint] (2022). https://doi.org/10.1101/2021.10.04.463034 (Accessed 1 June 2023).
61. E. F. Pettersen *et al.*, UCSF ChimeraX: Structure visualization for researchers, educators, and developers. *Protein Sci. Publ. Protein Soc.* **30**, 70–82 (2021).
62. M. Haon *et al.*, Recombinant protein production facility for fungal biomass-degrading enzymes using the yeast *Pichia pastoris*. *Front. Microbiol.* **6**, 1002 (2015).
63. M. Couturier *et al.*, Lytic xylan oxidases from wood-decay fungi unlock biomass degradation. *Nat. Chem. Biol.* **14**, 306–310 (2018).
64. K. Manalastas-Cantos *et al.*, ATSAS 3.0: Expanded functionality and new tools for small-angle scattering data analysis. *J. Appl. Crystallogr.* **54**, 343–355 (2021).
65. P. V. Konarev, D. I. Svergun, A posteriori determination of the useful data range for small-angle scattering experiments on dilute monodisperse systems. *IUCrJ* **2**, 352–360 (2015).
66. A. Guinier, La diffraction des rayons X aux très petits angles: Application à l'étude de phénomènes ultramicroscopiques. *Ann. Phys.* **11**, 161–237 (1939).
67. A. Guinier, G. Fournet, C. B. Walker, G. H. Vineyard, Small-angle scattering of X-rays. *Phys. Today* **9**, 38–39 (1956).
68. D. Franke, C. M. Jeffries, D. I. Svergun, Correlation Map, a goodness-of-fit test for one-dimensional X-ray scattering spectra. *Nat. Methods* **12**, 419–422 (2015).
69. P. Bernadó, M. Blackledge, A self-consistent description of the conformational behavior of chemically denatured proteins from NMR and small angle scattering. *Biophys. J.* **97**, 2839–2845 (2009).
70. D. K. Wilkins *et al.*, Hydrodynamic radii of native and denatured proteins measured by pulse field gradient NMR techniques. *Biochemistry* **38**, 16424–16431 (1999).
71. G. Tria, H. D. T. Mertens, M. Kachala, D. I. Svergun, Advanced ensemble modelling of flexible macromolecules using X-ray solution scattering. *IUCrJ* **2**, 207–217 (2015).
72. R. Kittl, D. Kracher, D. Burgstaller, D. Haltrich, R. Ludwig, Production of four *Neurospora crassa* lytic polysaccharide monooxygenases in Pichia pastoris monitored by a fluorimetric assay. *Biotechnol. Biofuels* **5**, 79 (2012).
73. E. Breslmayr *et al.*, A fast and sensitive activity assay for lytic polysaccharide monooxygenase. *Biotechnol. Biofuels* **11**, 79 (2018).
74. G. Tsuji, S. Fujii, S. Tsuge, T. Shiraishi, Y. Kubo, The *Colletotrichum lagenarium* Ste12-like gene CST1 is essential for appressorium penetration. *Mol. Plant Microbe Interact.* **16**, 315–325 (2003).
75. S. Kodama, T. Nishiuchi, Y. Kubo, Colletotrichum orbiculare MTF4 is a key transcription factor downstream of MOR essential for plant signal-dependent appressorium development and pathogenesis. *Mol. Plant Microbe Interact.* **32**, 313–324 (2019).
76. P. Gan, K. Shirasu, Endoglucanase-7 [Colletotrichum orbiculare MAFF 240422]. GenBank. https://www.ncbi.nlm.nih.gov/protein/TDZ22550. Accessed 10 January 2022.
77. P. Gan, K. Shirasu, Endoglucanase-4 [Colletotrichum orbiculare MAFF 240422]. GenBank. https://www.ncbi.nlm.nih.gov/protein/TDZ14194. Accessed 10 January 2022.
78. P. Gan, K. Shirasu, putative endo-beta-1,4-glucanase D [Colletotrichum orbiculare MAFF 240422]. GenBank. https://www.ncbi.nlm.nih.gov/protein/TDZ20118. Accessed 10 January 2022.
79. P. Gan, K. Shirasu, Endo-beta-1,4-glucanase D [Colletotrichum orbiculare MAFF 240422]. GenBank. https://www.ncbi.nlm.nih.gov/protein/TDZ16196. Accessed 10 January 2022.
80. P. Gan, K. Shirasu, Endoglucanase-7 [Colletotrichum orbiculare MAFF 240422]. GenBank. https://www.ncbi.nlm.nih.gov/protein/TDZ26868. Accessed 10 January 2022.
81. P. Gan, K. Shirasu, putative endo-beta-1,4-glucanase D [Colletotrichum orbiculare MAFF 240422]. GenBank. https://www.ncbi.nlm.nih.gov/protein/TDZ18990. Accessed 10 January 2022.
82. P. Gan, K. Shirasu, putative endo-beta-1,4-glucanase D [Colletotrichum orbiculare MAFF 240422]. GenBank. https://www.ncbi.nlm.nih.gov/protein/TDZ20143. Accessed 10 January 2022.
83. P. Gan, K. Shirasu, putative endo-beta-1,4-glucanase D [Colletotrichum orbiculare MAFF 240422]. GenBank. https://www.ncbi.nlm.nih.gov/protein/TDZ22880. Accessed 10 January 2022.
84. P. Gan, K. Shirasu, Polysaccharide monooxygenase Cel61a [Colletotrichum orbiculare MAFF 240422]. GenBank. https://www.ncbi.nlm.nih.gov/protein/TDZ15358. Accessed 10 January 2022.
85. P. Gan, K. Shirasu, putative endo-beta-1,4-glucanase D [Colletotrichum orbiculare MAFF 240422]. GenBank. https://www.ncbi.nlm.nih.gov/protein/TDZ24660. Accessed 10 January 2022.
86. P. Gan, K. Shirasu, Endo-beta-1,4-glucanase D [Colletotrichum orbiculare MAFF 240422]. GenBank. https://www.ncbi.nlm.nih.gov/protein/TDZ21771. Accessed 10 January 2022.
87. P. Gan, K. Shirasu, Polysaccharide monooxygenase Cel61a [Colletotrichum orbiculare MAFF 240422]. GenBank. https://www.ncbi.nlm.nih.gov/protein/TDZ24176. Accessed 10 January 2022.
88. P. Gan, K. Shirasu, Cellulose-growth-specific protein [Colletotrichum orbiculare MAFF 240422]. GenBank. https://www.ncbi.nlm.nih.gov/protein/TDZ15044. Accessed 10 January 2022.
89. P. Gan, K. Shirasu, Endoglucanase-4 [Colletotrichum orbiculare MAFF 240422]. GenBank. https://www.ncbi.nlm.nih.gov/protein/TDZ16734. Accessed 10 January 2022.
90. P. Gan, K. Shirasu, Endoglucanase-4 [Colletotrichum orbiculare MAFF 240422]. GenBank. https://www.ncbi.nlm.nih.gov/protein/TDZ25977. Accessed 10 January 2022.
91. P. Gan, K. Shirasu, putative endo-beta-1,4-glucanase D [Colletotrichum orbiculare MAFF 240422]. GenBank. https://www.ncbi.nlm.nih.gov/protein/TDZ17686. Accessed 10 January 2022.
92. P. Gan, K. Shirasu, putative endo-beta-1,4-glucanase D [Colletotrichum orbiculare MAFF 240422]. GenBank. https://www.ncbi.nlm.nih.gov/protein/TDZ18310. Accessed 10 January 2022.
93. P. Gan, K. Shirasu, Polysaccharide monooxygenase Cel61a [Colletotrichum orbiculare MAFF 240422]. GenBank. https://www.ncbi.nlm.nih.gov/protein/TDZ25475. Accessed 10 January 2022.
94. P. Gan, K. Shirasu, putative endo-beta-1,4-glucanase D [Colletotrichum orbiculare MAFF 240422]. GenBank. https://www.ncbi.nlm.nih.gov/protein/TDZ16856. Accessed 10 January 2022.
95. P. Gan, K. Shirasu, Endoglucanase-4 [Colletotrichum orbiculare MAFF 240422]. GenBank. https://www.ncbi.nlm.nih.gov/protein/TDZ21897. Accessed 10 January 2022.
96. P. Gan, K. Shirasu, Polysaccharide monooxygenase Cel61a [Colletotrichum orbiculare MAFF 240422]. GenBank. https://www.ncbi.nlm.nih.gov/protein/TDZ25610. Accessed 10 January 2022.
97. P. Gan, K. Shirasu, putative endo-beta-1,4-glucanase D [Colletotrichum orbiculare MAFF 240422]. GenBank. https://www.ncbi.nlm.nih.gov/protein/TDZ16420. Accessed 10 January 2022.
98. P. Gan, K. Shirasu, putative endo-beta-1,4-glucanase D [Colletotrichum orbiculare MAFF 240422]. GenBank. https://www.ncbi.nlm.nih.gov/protein/TDZ13877. Accessed 10 January 2022.
99. P. Gan, K. Shirasu, putative endo-beta-1,4-glucanase D [Colletotrichum orbiculare MAFF 240422]. GenBank. https://www.ncbi.nlm.nih.gov/protein/TDZ14609. Accessed 10 January 2022.
100. P. Gan, K. Shirasu, Polysaccharide monooxygenase Cel61a [Colletotrichum orbiculare MAFF 240422]. GenBank. https://www.ncbi.nlm.nih.gov/protein/TDZ15802. Accessed 10 January 2022.
101. P. Gan, K. Shirasu, putative endo-*beta*-1,4-glucanase D [Colletotrichum orbiculare MAFF 240422]. GenBank. https://www.ncbi.nlm.nih.gov/protein/TDZ14497. Accessed 10 January 2022.
102. P. Gan, K. Shirasu, Glycosyl hydrolase family 61 [Colletotrichum higginsianum IMI 349063]. GenBank. https://www.ncbi.nlm.nih.gov/protein/XP_018155356.1. Accessed 10 January 2022.
103. P. Gan, K. Shirasu, Endoglucanase-4 [Colletotrichum higginsianum IMI 349063]. GenBank. https://www.ncbi.nlm.nih.gov/protein/XP_018155797. Accessed 10 January 2022.
104. A. G. Kikhney, C. R. Borges, D. S. Molodenskiy, C. M. Jeffries, D. I. Svergun, SASBDB: Towards an automatically curated and validated repository for biological scattering data. *Protein Sci.* **29**, 66-75 (2019).
105. K. C. Tamburrini, S. Longhi, J. G. Berrin, SASDUG3 – *Colletotrichum orbiculare* Auxiliary Activity Family 9A Lytic Polysaccharide Monooxygenase (AA9A LPMO) monomer. SASDB.https://www.sasbdb.org/data/SASDUG3. Deposited 19 February 2024.
106. K. C. Tamburrini, S. Longhi, J. G. Berrin, SASDUH3 – *Colletotrichum orbiculare* Auxiliary Activity Family 9A Lytic Polysaccharide Monooxygenase (AA9A LPMO) dimer. SASDB.https://www.sasbdb.org/data/SASDUH3. Deposited 19 February 2024.
107. K. C. Tamburrini, S. Longhi, J. G. Berrin, SASDUJ3 – *Colletotrichum orbiculare* Auxiliary Activity Family 9A Lytic Polysaccharide Monooxygenase (AA9A LPMO) deltaX283. SASDB. https://www.sasbdb.org/data/SASDUJ3. Deposited 19 February 2024.
108. K. C. Tamburrini, S. Longhi, J. G. Berrin, SASDUK3 – *Colletotrichum orbiculare* Auxiliary Activity Family 9A Lytic Polysaccharide Monooxygenase (AA9A LPMO) C286A*. SASDB. https://www.sasbdb.org/data/SASDUK3. Deposited 19 February 2024.
109. K. C. Tamburrini, S. Longhi, J. G. Berrin, SASDUL3 – *Colletotrichum higginsianum* Auxiliary Activity Family 9A Lytic Polysaccharide Monooxygenase (AA9A LPMO) monomer. SASDB. https://www.sasbdb.org/data/SASDUL3. Deposited 19 February 2024.
110. K. C. Tamburrini, S. Longhi, J. G. Berrin, SASDUM3 – *Colletotrichum higginsianum* Auxiliary Activity Family 9A Lytic Polysaccharide Monooxygenase (AA9A LPMO) dimer. SASDB. https://www.sasbdb.org/data/SASDUM3. Deposited 19 February 2024.
111. K. C. Tamburrini, S. Longhi, J. G. Berrin, SASDUN3 – *Colletotrichum higginsianum* Auxiliary Activity Family 9B Lytic Polysaccharide Monooxygenase (AA9B LPMO) monomer. SASDB. https://www.sasbdb.org/data/SASDUN3. Deposited 19 February 2024.
112. K. C. Tamburrini, S. Longhi, J. G. Berrin, SASDUP3 – *Colletotrichum higginsianum* Auxiliary Activity Family 9B Lytic Polysaccharide Monooxygenase (AA9B LPMO) dimer. SASDB. https://www.sasbdb.org/data/SASDUP3. Deposited 19 February 2024.
113. H. Ghafouri *et al.*, PED in 2024: improving the community deposition of structural ensembles for intrinsically disordered proteins. *Nucleic Acids Res.* **52**, D536-D544 (2023).
114. K. C. Tamburrini, S. Longhi, J. G. Berrin, SAXS-derived ensemble of the dimeric AA9A LPMO from Colletotrichum orbiculare. https://proteinensemble.org/entries/PED00506. Deposited 27 February 2024.